A Novel Strongly Spin-Orbit Coupled Quantum Dimer Magnet: $Yb_2Si_2O_7$

Gavin Hester,[1,*] H. S. Nair,[1] T. Reeder,[1] D. R. Yahne,[1] T. N. DeLazzer,[1] L. Berges,[2] D. Ziat,[2] J. A. Quilliam,[2] J. R. Neilson,[3] A. A. Aczel,[4] G. Sala,[4] and K. A. Ross[1,5,†]

[1]*Department of Physics, Colorado State University, 200 W. Lake St., Fort Collins, CO 80523-1875, USA*
[2]*Institut Quantique and Département de Physique, Université de Sherbrooke, 2500 boulevard de l'Université, Sherbrooke, Québec J1K 2R1, Canada*
[3]*Department of Chemistry, Colorado State University, 200 W. Lake St., Fort Collins, CO 80523-1872, USA*
[4]*Oak Ridge National Laboratory, Oak Ridge, TN 37830, USA*
[5]*Quantum Materials Program, Canadian Institute for Advanced Research (CIFAR), Toronto, Ontario M5G 1Z8, Canada*

(Dated: July 18, 2022)

The quantum dimer magnet (QDM) is the canonical example of "quantum magnetism". The QDM state consists of entangled nearest-neighbor spin dimers and often exhibits a field-induced "triplon" Bose-Einstein condensate (BEC) phase. We report on a new QDM in the strongly spin-orbit coupled, distorted honeycomb-lattice material $Yb_2Si_2O_7$. Our single crystal neutron scattering, specific heat, and ultrasound velocity measurements reveal a gapped singlet zero field ground state with sharp, dispersive excitations. We find a field-induced magnetically ordered phase reminiscent of a BEC phase, with exceptionally low critical fields of $H_{c1} \sim 0.4$ T and $H_{c2} \sim 1.4$ T. Using inelastic neutron scattering in an applied magnetic field we observe a Goldstone mode (gapless to within δE = 0.037 meV) that persists throughout the entire field-induced magnetically ordered phase, suggestive of the spontaneous breaking of U(1) symmetry expected for a triplon BEC. However, in contrast to other well-known cases of this phase, the high-field ($\mu_0 H \geq 1.2$T) part of the phase diagram in $Yb_2Si_2O_7$ is interrupted by an unusual regime signaled by a change in the field dependence of the ultrasound velocity and magnetization, as well as the disappearance of a sharp anomaly in the specific heat. These measurements raise the question of how anisotropy in strongly spin-orbit coupled materials modifies the field induced phases of QDMs.

arXiv:1810.13096v1 [cond-mat.str-el] 31 Oct 2018

Quantum dimer magnets (QDMs) represent the simplest cases of "quantum magnetism", where entanglement is a required ingredient for even a qualitative understanding of the phase. In a QDM, entangled pairs of spins form $S_{tot} = 0$ dimers and result in a non-magnetic ground state. The excited states of these entangled spins can be treated as bosons, called "triplons", which can undergo Bose-Einstein condensation (BEC) as their density is tuned by an applied magnetic field. This BEC state is a magnetic field-induced long range ordered phase, which occupies a symmetric "dome" in the field vs. temperature phase diagram with two temperature-dependent critical fields, $H_{c1}(T)$ and $H_{c2}(T)$. The vast majority of the previously studied QDMs are based on 3d transition metal ions with "bare" (spin-only) $S = 1/2$ or $S = 1$ angular momentum, resulting in simple Heisenberg or XXZ spin interaction Hamiltonians, and high critical fields set by the relatively high energy scale of exchange interactions [1–6].

Recently, it has become more widely appreciated that lanthanide-based magnetic materials with spin-orbit coupled pseudo-spin 1/2 (S_{eff}= 1/2) angular momenta can exhibit quantum phases, which are often directly analogous to their traditional 3d transition metal ion counterparts. However, sometimes entirely new phases are possible, such as Quantum Spin Ice [7–10] or the Kitaev spin liquid [11, 12], due to the anisotropic exchange in these materials. In the lanthanide series, Yb^{3+} has been of particular interest as it can generically host interactions leading to quantum fluctuations irrespective of the Crystal Electric Field (CEF) ground state doublet composition [13]. Indeed, various quantum phases have been discovered in Yb-based systems; from the strong quantum fluctuations and unusual continuum-like excitations in the Yb pyrochlores $Yb_2B_2O_7$ (B=Ti,Ge,Sn) [9, 14, 15], to one-dimensional S_{eff}=1/2 spin chains with spinon excitations in Yb_2Pt_2Pb [16], to quantum tetramers in the breathing pyrochlore $Ba_3Yb_2Zn_5O_{11}$ [17]. However, a notable absence is a material exhibiting a QDM with a field-induced BEC state, the canonical example of quantum magnetism. The opportunity to study such a material could lead to the observation of new phases describable by theories of interacting bosons, as well as new types of quantum phase transitions.

As a previously studied example, the metallic material $YbAl_3C_3$ was shown to host Yb dimerization and triplet excitations [18, 19]. However, an unusual field-induced ordered state was observed whose onset temperature far exceeds the spin gap energy [20], suggesting that it is not directly related to the singlet-triplet excitation (unlike a field-induced BEC phase). Additionally, $YbAl_3C_3$ shows field-induced *disordered* regimes that have yet to be fully understood, particularly in the context of the additional Kondo and RKKY interactions involving the conduction electrons in this material [21–23]. This material demonstrates that quantum dimerization is possible in lanthanide-based magnetic materials, but does not always lead to a field-induced BEC phase. Naively, one might not expect a highly spin-orbit coupled material to exhibit BEC, which requires the exchange Hamiltonian to be at least U(1) symmetric (i.e., XXZ type interactions). Although recent work has demonstrated that for ideal, edge-sharing octahedral environments, Heisenberg exchange is indeed dominant in Yb materials [13], such high exchange symmetry is not *a priori* expected for non-ideal local environments. This gives rise to the question of how exchange anisotropy might modify both the QDM ground state and the field-induced phases. Furthermore, lanthanide-based QDMs should provide a convenient testing ground of field-induced BEC physics due to reduced exchange energy compared to 3d transition metal based materials. This leads to lower critical fields, which can be accessed by continuous field magnets, thus enabling experimental techniques such as inelastic neutron scattering (INS) to be brought to bear on the full phase diagram. This is the case for $Yb_2Si_2O_7$, as we show here.

$Yb_2Si_2O_7$ (monoclinic space group C2/m, room temperature lattice parameters of a =6.7714(9)Å, b = 8.8394(2)Å, c =4.6896(5)Å, β = 101.984(9)° [24]) was previously studied in the context of polymorphism in the $RE_2Si_2O_7$ (rare earth

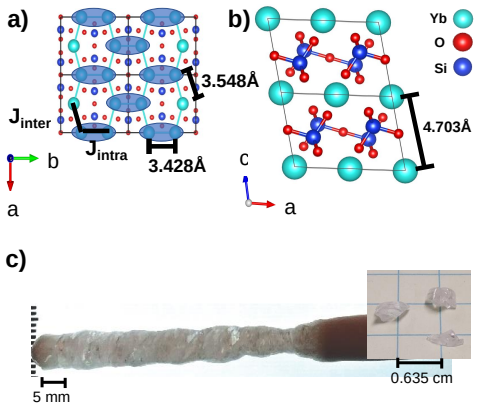

FIG. 1: a) Crystal structure of $Yb_2Si_2O_7$ viewed along the c-axis, where Yb atoms are light green and form a distorted honeycomb lattice, Si atoms are blue, and O atoms are red. Intradimer (3.428Å) and interdimer (3.548Å) bond lengths are shown (3% anisotropy). The intradimer (J_{intra}) and interdimer (J_{inter}) exchange tensors are labeled. The blue ovals indicate the probable location of the dimers. b) Crystal structure viewed along the b-axis, showing the separation of the layers of Yb honeycombs. c) A picture of an as-grown crystal boule. The opacity of the bulk is due to the crystal cracking during cooling. (inset) Characteristic crystals obtained from breaking the crystal boule. The crystals are clear and colorless.

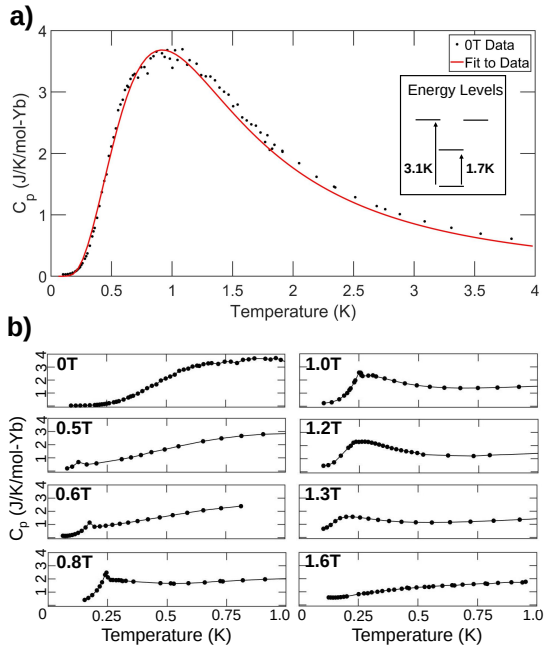

FIG. 2: a) Zero-field specific heat and fit to a 4-level Schottky anomaly. The fit was constrained to be consistent with XXZ symmetry (a singlet and doublet excited states). The extracted energy levels (1.7, 3.1, 3.1 K) are only approximate, as the fit does not take into account the dispersion of the excited states. b) Specific heat of $Yb_2Si_2O_7$ at increasing fields with $H||c$. A sharp anomaly is visible at 0.5 T ($>H_{c1}$), which is due to a field-induced magnetically ordered state based on our neutron scattering data. The transition temperature maps out a dome as a function of field, but the sharp anomaly is replaced by a broad anomaly above $\sim$ 1.2 T (H_m), which moves to lower temperatures with increasing field. Above H_{c2}(1.4 T), the broad anomaly shifts to higher temperatures with increasing field, consistent with field polarized paramagnetism.

pyrosilicate) series [25, 26], but its magnetic properties have not been reported. $Yb_2Si_2O_7$ has only one reported polymorph, known as the C-type pyrosilicate (Fig. 1). The single crystal samples of $Yb_2Si_2O_7$ used in this study were grown via the optical floating zone method [24]. Our growths have resulted in clear, colorless multi-crystal boules which are then broken into smaller single crystal pieces as shown in Fig. 1c.

Magnetization was measured using a MPMS X5 Quantum Design SQUID magnetometer at $T = 1.8$ K along the a^*, b^*, and c directions. Field- and temperature-dependent specific heat was measured down to 50 mK using the quasi-adiabatic heat pulse method in a Quantum Design Dynacool PPMS with a dilution refrigerator insert. $Lu_2Si_2O_7$ was also measured as a non-magnetic analog. Ultrasound velocity experiments were performed down to 50 mK using a pulsed, time-of-flight interferometer. 30 MHz transducers were glued to parallel surfaces so as to propagate longitudinally polarized sound waves along the c^*-axis. The absolute velocity of the quasi-longitudinal mode studied here was approximately 3000 m/s and relative changes in velocity ($\Delta v/v$) were measured with high precision using a phase-lock loop. Powder neutron diffraction data was collected on BT1 at the NIST Center for Neutron Research with incident wavelength $\lambda = 2.0787$ Å and 60 arcminute collimation. Synchrotron x-ray diffraction (SXRD) data were recorded at $T = 295$ K at beamline 11 BM (λ = 0.41418 Å) at the Advanced Photon Source, Argonne National Laboratory. Time-of-flight INS experiments were performed at the Cold Neutron Chopper Spectrometer (CNCS) at the Spallation Neutron Source, Oak Ridge National Laboratory (ORNL). These INS data were collected using E_i = 1.55 meV neutrons in the "high flux" chopper setting mode, producing an energy resolution of δE = 0.037 meV at the elastic line [27]. A neutron diffraction measurement using $E_i = 14.7$ meV neutrons was performed using the Fixed-Incident Energy Triple-Axis Spectrometer (FIE-TAX) on the HB-1A beamline at the High Flux Isotope Reactor at Oak Ridge National Laboratory, using collimator settings of 40' - 40' - 40' - 80'.

Rietveld analysis of the SXRD data [24] confirms the previously reported crystal structure. Analysis of the zero field magnetic specific heat of $Yb_2Si_2O_7$ confirms that a low energy S_{eff}=1/2 picture applies at temperatures well below $\sim$ 100 K [24]. The saturation magnetization at $T = 1.8$ K along three crystal directions gives the approximate g-values of $g_{a*} = 3.2$, $g_{b*} = 2.0$, and $g_c = 4.8$.

The zero-field specific heat shown in Fig. 2a displays a broad feature peaked at $\sim$ 1 K, which can be fit to a 4-level Schottky anomaly form, consistent with a spin dimer ground state. The energy level splittings (ΔE = 1.7, 3.1, 3.1 K) were extracted by enforcing the singlet and doublet excited state structure that is implied by XXZ symmetry, which was motivated by the INS results, as discussed below. The inferred 1.7K (0.15 meV) excited singlet level is on the same order as the gap to the excited state observed by INS (0.1162(4) meV). Within the isolated dimer model, these extracted splittings imply the XXZ exchange interactions $J^{XX}_{\text{intra}} = 1.7$ K, J^{Z}_{intra} = 4.5 K. However, the ΔE values (and hence, J_{intra} values) determined this way are only approximate, as this model does not take into account the strong dispersion of the excited states (Fig. 4a), which implies significant interdimer exchange. The entropy change through this low temperature Schottky anomaly (0.05 to 2 K), reaches the expected Rln2 per Yb [24], indicating

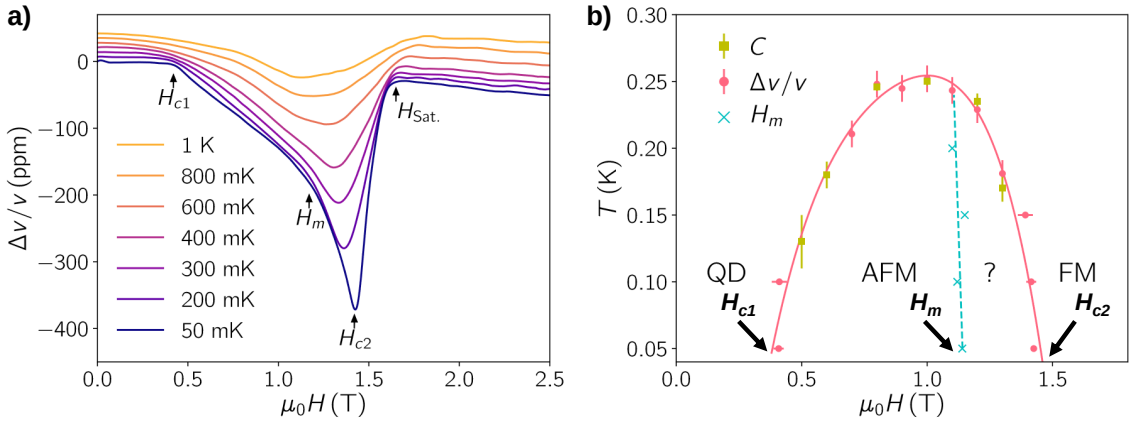

FIG. 3: a) Ultrasound velocity with longitudinally polarized sound waves along the c^*-axis. b) A H vs. T phase diagram for $Yb_2Si_2O_7$ with the points on the phase boundary determined by ultrasound velocity (pink circles and blue crosses) and specific heat (yellow squares). The field was applied along the c-axis (specific heat) and c^*-axis (ultrasound).

that $Yb_2Si_2O_7$ does not undergo a magnetic ordering transition at lower temperatures, and thus remains quantum disordered down to $T = 0$ K. This is further confirmed by the lack of magnetic Bragg peaks at 50 mK, as determined by both single crystal (Fig. 4c) and powder neutron diffraction measurements [24].

The field-dependence ($H||c$) of the specific heat is shown in Fig. 2b. At $H = 0.5$ T, a sharp anomaly appears at $T = 0.13$ K, which we have confirmed by neutron scattering to coincide with a transition to long range magnetic order via the appearance of magnetic Bragg peaks. With increasing field, the transition temperature maps out a "dome" in the H vs. T phase diagram as expected for a BEC phase. As the field is increased further ($\sim$ 0.8T), a broad feature emerges, which eventually becomes the dominant feature above $H_m = 1.2$ T. The maximum of this broad feature then continues to trace out the high field region of the dome, with the temperature of the maximum decreasing with increasing field. At 1.6 T, the maximum of the broad feature is again increasing in temperature with increasing field as expected for a field-polarized paramagnetic regime.

Isothermal field scans of variations in sound velocity are shown in Fig. 3a for various temperatures. At the lowest temperatures ($T = 50$ mK) the sound velocity is largely field independent until $H_{c1} \simeq 0.4$ T, where $\Delta v/v$ begins decreasing with field. At $H_{c2} \simeq 1.4$ T, $\Delta v(H)$ reaches a minimum, before returning sharply to roughly the zero field value in the field polarized limit. In addition to the two expected critical fields, H_{c1} and H_{c2}, the sound velocity also exhibits a significant change in slope at roughly $H_m = 1.2$ T, suggesting the presence of an additional phase, as indicated in Fig. 3b. Aside from the sharp change of slope at H_m, our sound velocity measurements resemble those performed on another quantum dimer magnet, $Sr_3Cr_2O_8$ [28]. In contrast, sound velocity measurements on $NiCl_2$-$4SC(NH_2)_2$ [29] show sharper dips at both H_{c1} and H_{c2}, which are attributed to coupling between the ultrasound velocity and antiferromagnetic fluctuations.

As the temperature is raised, the overall variations in sound velocity become much smaller in magnitude and the sharp features are smoothed out, hence we use temperature scans of sound velocity (see Supplemental Information [24]), which show small but fairly sharp anomalies, to establish the phase boundaries of the antiferromagnetic dome at higher temperatures. These boundaries are entirely consistent with the specific heat measurements.

The dome of field-induced order mapped out by the specific heat and ultrasound velocity data (Fig. 3b) is similar to the BEC phase of traditional QDMs, but there is an important difference: the dome in $Yb_2Si_2O_7$ is asymmetric, with an unusual regime in the high field part of the phase ($H > H_m$). The asymmetry of the dome may be due to non-XXZ terms in the S_{eff}=1/2 low energy effective Hamiltonian for $Yb_2Si_2O_7$. However, the strength of any anisotropic exchange (non-XXZ terms) is limited by our observation of a Goldstone mode (gapless to within $\delta E = 0.037$ meV) via INS, discussed below.

Inelastic neutron scattering data provides evidence of the spontaneous breaking of an approximately continuous symmetry for fields between H_{c1} and H_{c2}. Fig. 4a shows the excitations of $Yb_2Si_2O_7$ along the [0.1K0] direction at $T = 50$ mK for representative applied fields, while Fig. 4b shows the field evolution of a cut at (-0.25,0,0), close to (but not exactly at) the (0,0,0) zone center. In a QDM with Heisenberg exchange, the three excited dimer states are triply degenerate (forming a triplet with $S_{tot} = 1$, and $S_z = -1, 0$, and 1), and are then Zeeman split by the applied magnetic field. With finite interdimer exchange the resulting triplons are mobile, and the excited states become dispersive. For $Yb_2Si_2O_7$ below H_{c1} a resolution-limited single excited dispersive branch (bandwidth of 0.167(1) meV, and a gap of 0.1162(4) meV) is visible. The apparent secondary branch observed for negative K values is due to a minority crystal grain, as discussed in the Supplemental Information [24]. The energy of the excitation does not change for $H < H_{c1}$ (Fig. 4b), signifying that the angular momentum projection along the magnetic field is zero (i.e., S_{tot} = 1, S_z = 0, which we call ψ_0). The absence of the $S_{tot} = 1$, $S_z \pm 1$ states (hereafter labeled as $\psi_{\pm 1}$) in the spectrum indicates that the neutron scattering transition matrix elements from the ground state to $\psi_{\pm 1}$ are small compared to that for ψ_0. This is as expected if the CEF ground state doublet does not have strong transition matrix elements for J_+ and J_- [24]. Above H_{c1}, a new low energy excitation appears, which is gapless at the magnetic zone centers to within the energy resolution of the instrument ($\delta E = 0.037$ meV). This Goldstone mode implies spontaneous breaking of an approxi-

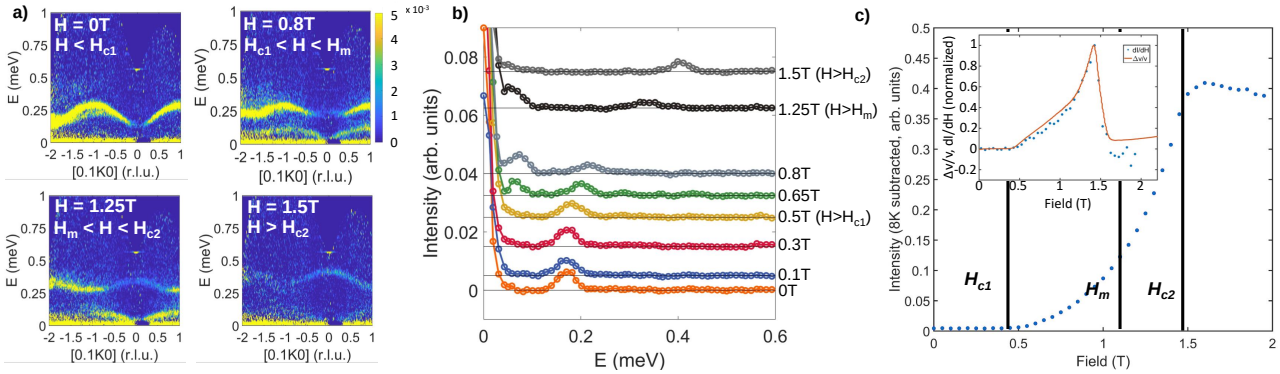

FIG. 4: a) Inelastic neutron scattering data at $T = 50$ mK along the [0.1K0] direction (slightly off of [0K0] to illustrate behavior near [000]: integrated from H = -0.2 to H = 0) for representative fields applied along the c axis. Between $H_{c1}$and H_{c2}, a Goldstone mode appears (gapless to within the energy resolution of the instrument, δE = 0.037 meV). b) Cuts of the inelastic neutron spectrum at (-0.25, 0, 0), integrating over H = [-0.3,-0.2] and K = [-0.1,0.1] r.l.u. The excitation branch leading to the Goldstone mode is visible as a low energy peak between H_{c1} and H_{c2}. Below H_{c1}, the peak near 0.19 meV remains at constant energy, identifying it as a $S_z = 0$ excitation (ψ_0). c) Evolution of the (2,0,0) magnetic Bragg peak intensity versus field, $I(H)$, which is proportional to the square of the net magnetization ($I \propto M^2$). Inset: An overlay of $\frac{dI}{dH} = 2M\chi_{zz}$ and the negative of the ultrasound velocity data, showing agreement between these two measurements.

mate U(1) symmetry in the plane perpendicular to the applied magnetic field (the a^*-b^* plane), suggestive of the BEC transition observed in traditional QDMs [1, 30]. Here we note that the energy resolution is 25% of J^{XX}_{intra} estimated based on the Schottky fit to the specific heat, thus this measurement of the "Goldstone" mode actually allows for a potentially sizable anisotropic exchange contribution. Perhaps related to this, the "Goldstone" mode persists between H_m and H_{c2}, despite the lack of evidence for spontaneous symmetry breaking in $C_p(T)$ in this field range (i.e. a sharp anomaly is absent). However, the broad $C_p(T)$ feature moves to lower temperature as the field is further increased. This, combined with the continued presence of the Goldstone mode, are contrary to the expectation for a field-polarized paramagnet. In contrast, above H_{c2} all of the excitations become fully gapped, consistent with a field-polarized paramagnet. In the field polarized regime, the inelastic intensity is greatly reduced due to the development of strong magnetic Bragg peaks at the elastic line, as expected based on the sum rule for neutron scattering.

Fig. 4c shows the field dependence of neutron diffraction (measured on FIE-TAX) at the (2,0,0) zone center. This reflection is only sensitive to the square of the net magnetization (m_z^2) that arises due to canting towards the field direction, rather than any AFM components of the magnetic structure. The onset of magnetic order and growth of the net magnetization is confirmed above H_{c1} through the observation of increasing magnetic Bragg peak intensity. The intensity of the (2,0,0) peak shows an approximately quadratic increase, with a sudden change in the second derivative occurring at approximately H_m. The inset to Fig. 4c shows a comparison of the first derivative of the (2,0,0) Bragg peak intensity at 50 mK and the negative of the relative ultrasound velocity at 100 mK, which are consistent (though this level of agreement is somewhat unexpected following a standard theoretical treatment, see [24]).

$Yb_2Si_2O_7$ is structurally similar to the famous Kitaev material Na_2IrO_3 [31] as they share the same space group and Wyckoff position of the magnetic species. Therefore, Kitaev exchange is allowed by symmetry in $Yb_2Si_2O_7$. If this exchange interaction were dominant, it could lead to a quantum spin liquid ground state [11]. The presence of a Goldstone mode rules out dominant Kitaev exchange in $Yb_2Si_2O_7$, but it may still occur at the $\sim 25\%$ level, and it might be possible to increase the strength of such interactions by physical pressure or chemical substitution.

In summary, the strongly spin-orbit coupled material $Yb_2Si_2O_7$ realizes a QDM ground state with magnetic field-induced order reminiscent of a BEC phase. However, this ordered phase exhibits unusual characteristics at the high field part of the dome, including an abrupt change in the field dependence of the magnetization, and the loss of a sharp anomaly in the specific heat. The presence of a Goldstone mode throughout the full field-induced ordered state suggests dominant XXZ exchange interactions. However, the observation of the unusual regime between H_m and H_{c2} may imply that additional anisotropic interactions are necessary in order to fully describe the field induced phases of this novel quantum magnet. $Yb_2Si_2O_7$ provides the first example of a Yb^{3+}-based QDM with a possible field-induced BEC phase, adding this canonical example of quantum magnetism to the roster of quantum phases exhibited by materials based on this versatile ion.

This research was supported by the National Science Foundation Agreement No. DMR-1611217. The authors acknowledge the assistance of Aaron Glock and Antony Sikorski in the sample synthesis, as well as Craig Brown for his assistance with the BT1 neutron powder diffraction experiment. A portion of this work used resources at the Spallation Neutron Source and High Flux Isotope Reactor, which are DOE Office of Science User Facilities operated by Oak Ridge National Laboratory. The authors also acknowledge the support of the National Institute of Standards and Technology, US Department of Commerce in providing some of the neutron research facilities used in this work.

* Electronic address: Gavin.Hester@colostate.edu
† Electronic address: Kate.Ross@colostate.edu

[1] V. Zapf, M. Jaime, and C. D. Batista, Reviews of Modern Physics **86**, 563 (2014).

[2] V. S. Zapf, D. Zocco, B. R. Hansen, M. Jaime, N. Harrison, C. D. Batista, M. Kenzelmann, C. Niedermayer, A. Lacerda, and A. Paduan-Filho, Physical Review Letters **96**, 1 (2006), ISSN 00319007, 0505562.

[3] M. Jaime, V. F. Correa, N. Harrison, C. D. Batista, N. Kawashima, Y. Kazuma, G. A. Jorge, R. Stern, I. Heinmaa, S. A. Zvyagin, et al., Physical Review Letters **93**, 6 (2004), ISSN 00319007, 0404324.

[4] E. C. Samulon, Y. J. Jo, P. Sengupta, C. D. Batista, M. Jaime, L. Balicas, and I. R. Fisher, Physical Review B - Condensed Matter and Materials Physics **77**, 1 (2008), ISSN 10980121, 0803.3830.

[5] A. A. Aczel, Y. Kohama, C. Marcenat, F. Weickert, M. Jaime, O. E. Ayala-Valenzuela, R. D. McDonald, S. D. Selesnic, H. A. Dabkowska, and G. M. Luke, Physical Review Letters **103**, 1 (2009), ISSN 00319007, 0908.3049.

[6] A. Aczel, Y. Kohama, M. Jaime, K. Ninios, H. B. Chan, L. Balicas, H. Dabkowska, and G. Luke, Physical Review B **79**, 100409 (2009).

[7] M. Hermele, M. P. Fisher, and L. Balents, Physical Review B **69**, 064404 (2004).

[8] S. Onoda and Y. Tanaka, Physical review letters **105**, 047201 (2010).

[9] K. A. Ross, L. Savary, B. D. Gaulin, and L. Balents, Physical Review X **1**, 021002 (2011).

[10] M. J. Gingras and P. A. McClarty, Reports on Progress in Physics **77**, 056501 (2014).

[11] A. Kitaev, Annals of Physics **321**, 2 (2006).

[12] G. Jackeli and G. Khaliullin, Physical review letters **102**, 017205 (2009).

[13] J. G. Rau and M. J. P. Gingras, Physical Review B **98**, 1 (2018).

[14] J. D. Thompson, P. A. McClarty, D. Prabhakaran, I. Cabrera, T. Guidi, and R. Coldea, Physical Review Letters **119**, 1 (2017).

[15] A. M. Hallas, J. Gaudet, N. P. Butch, M. Tachibana, R. S. Freitas, G. M. Luke, C. R. Wiebe, and B. D. Gaulin, Physical Review B **93**, 1 (2016).

[16] L. S. Wu, W. J. Gannon, I. A. Zaliznyak, A. M. Tsvelik, M. Brockmann, J.-S. Caux, M. S. Kim, Y. Qiu, J. R. D. Copley, G. Ehlers, et al., Science **352**, 1206 (2016).

[17] J. G. Rau, L. S. Wu, A. F. May, L. Poudel, B. Winn, V. O. Garlea, A. Huq, P. Whitfield, A. E. Taylor, M. D. Lumsden, et al., Physical Review Letters **116**, 1 (2016).

[18] A. Ochiai, T. Inukai, and T. Matsumura, Journal of the Physical Society of Japan **76** (2007).

[19] Y. Kato, M. Kosaka, H. Nowatari, Y. Saiga, A. Yamada, T. Kobiyama, S. Katano, K. Ohoyama, H. Suzuki, N. Aso, et al., Journal of the Physical Society of Japan **77** (2008).

[20] D. D. Khalyavin, D. T. Adroja, P. Manuel, A. Daoud-Aladine, M. Kosaka, K. Kondo, K. A. McEwen, J. H. Pixley, and Q. Si, Physical Review B **220406**, 1 (2013).

[21] Y. Nakanishi, F. Shichinomiya, M. Koseki, G. Koseki, R. Kashiwazaki, K. Deto, M. Nakamura, M. Yoshizawa, and M. Kosaka, Journal of Physics: Conference Series **400** (2012).

[22] K. Hara, S. Matsuda, E. Matsuoka, K. Tanigaki, A. Ochiai, S. Nakamura, T. Nojima, and K. Katoh, Physical Review B - Condensed Matter and Materials Physics **85**, 1 (2012).

[23] S. Kittaka, T. Sugiyama, Y. Shimura, T. Sakakibara, S. Matsuda, and A. Ochiai, Journal of the Korean Physical Society **62**, 2088 (2013).

[24] *See Supplemental Information*.

[25] J. Felsche, Journal of The Less-Common Metals **21**, 1 (1970).

[26] Y. I. Smolin and Y. F. Shepelev, Acta Crystallographica Section B **26**, 484 (1970).

[27] G. Ehlers, A. A. Podlesnyak, J. L. Niedziela, E. B. Iverson, and P. E. Sokol, Review of Scientific Instruments **82**, 085108 (2011).

[28] Z. Wang, D. L. Quintero-Castro, S. Zherlitsyn, S. Yasin, Y. Skourski, B. Islam, A. T. M. N. and. Lake, J. Deisenhofer, and A. Loidl, Phys. Rev. Lett. **116**, 147201 (2016).

[29] O. Chiatti, A. Sytcheva, J. Wosnitza, S. Zherlitsyn, A. A. Zvyagin, V. S. Zapf, M. Jaime, and A. Paduan-Filho, Phys. Rev. B **78**, 094406 (2008).

[30] T. Giamarchi, C. Rüegg, and O. Tchernyshyov, Nature Physics **4**, 198 (2008).

[31] S. Hwan Chun, J. W. Kim, J. Kim, H. Zheng, C. C. Stoumpos, C. D. Malliakas, J. F. Mitchell, K. Mehlawat, Y. Singh, Y. Choi, et al., Nature Physics **11**, 462 (2015).

Supplemental Information for "A Novel Strongly Spin-Orbit Coupled Quantum Dimer Magnet: $Yb_2Si_2O_7$"

Gavin Hester,[1] H. S. Nair,[1] T. Reeder,[1] D. R. Yahne,[1] T. N. DeLazzer,[1] L. Berges,[2]
D. Ziat,[2] J. A. Quilliam,[2] J. R. Neilson,[3] A. A. Aczel,[4] G. Sala,[4] and K. A. Ross[1,5]

[1]*Department of Physics, Colorado State University, 200 W. Lake St., Fort Collins, CO 80523-1875, USA*
[2]*Institut Quantique and Département de Physique, Université de Sherbrooke, 2500 boulevard de l'Université, Sherbrooke, Québec J1K 2R1, Canada*
[3]*Department of Chemistry, Colorado State University, 200 W. Lake St., Fort Collins, CO 80523-1875, USA*
[4]*Oak Ridge National Laboratory, Oak Ridge, TN 37830, USA*
[5]*Quantum Materials Program, Canadian Institute for Advanced Research (CIFAR), Toronto, Ontario M5G 1Z8, Canada*
(Dated: July 18, 2022)

arXiv:1810.13096v1 [cond-mat.str-el] 31 Oct 2018

SAMPLE PREPARATION

Polycrystalline $Yb_2Si_2O_7$ was synthesized by combining stoichiometric amounts of Yb_2O_3 and SiO_2, pressing under hydrostatic pressure of ∼480 kPa, and heating 4-5 times at 1350°C for 48 hours, with regrinding between heatings to promote reaction, until phase purity was achieved (as confirmed by powder x-ray diffraction in air). Sintered cylindrical rods with diameter of 8 mm were prepared from these powders for optical floating zone crystal growth. A Crystal Systems furnace (FZ-T-10000-H-VIII-VPO-PC) was used for the crystal growth. Multiple growths were performed to optimize the parameters. The most successful growths were performed with 1.5 kW lamps (71% power), with a growth rate of 5 mm/hr, under an atmosphere of flowing air (2L / min), with a counterrotation of the upper and lower rods of 20 rpm. Every growth resulted in cracked boules, which upon further study by Laue x-ray diffraction, were found to be multi-crystalline. The boules were broken into separate single crystals (typical size approximately $3 \times 3 \times 2$ mm^3) which were clear and colorless (see Fig. 1c of main text).

CRYSTAL ELECTRIC FIELD CONSIDERATIONS

The low point group symmetry of Yb^{3+} in $Yb_2Si_2O_7$ (C_2) leads to nine independent Steven's parameters in a crystal field Hamiltonian [1]. Determining these experimentally, for example by an inelastic neutron scattering measurement of the single ion energy levels, is an underdetermined problem, since such an experiment only gives access to three transitions (between the four Kramers doublets). Thus, the CEF ground state for $Yb_2Si_2O_7$ is experimentally unknown. However, our observations do restrict some of the properties of the CEF ground state. Perhaps most significantly, we find that the $\psi_{\pm1}$ modes are not visible via inelastic neutron scattering at E_i = 1.55 meV. This can be explained if the CEF ground state doublet for Yb^{3+} does not have a significant matrix element for transitions induced by J_+ or J_-. For example, a CEF ground state doublet that is composed primarily of a single $|J_z\rangle$ eigenstate (except $|J_z\rangle = \pm 1/2$), will have vanishingly small matrix elements to the excited $\psi_{\pm1}$ states, as discussed below.

Assuming XXZ symmetry for the intradimer interactions, the dimer eigenstates are given by:

$$
\begin{aligned}
|\psi_{0,0}\rangle &= \frac{1}{\sqrt{2}}(|\uparrow\downarrow\rangle - |\downarrow\uparrow\rangle) \\
|\psi_{1,+1}\rangle &= |\uparrow\uparrow\rangle \\
|\psi_{1,-1}\rangle &= |\downarrow\downarrow\rangle \\
|\psi_{1,0}\rangle &= \frac{1}{\sqrt{2}}(|\uparrow\downarrow\rangle + |\downarrow\uparrow\rangle)
\end{aligned}
$$

where the pseudo-spins can be identified as the CEF Kramer's doublet ground states $|\pm\rangle$, i.e., $|\uparrow\rangle = |+\rangle$ and $|\downarrow\rangle = |-\rangle$. These Kramer's doublet wavefunctions can be expressed as linear combinations of $\mathsf{J_z}$ eigenstates, $|J, M_J\rangle$, within a constant J manifold [2]:

$$
\begin{aligned}
|+\rangle &= \sum_{M_J=-J}^{J} C_{M_J}|J, M_J\rangle, \\
|-\rangle &= \sum_{M_J=-J}^{J} C^*_{M_J}(-1)^{J-M_J}|J, -M_J\rangle
\end{aligned}
$$

The neutron scattering intensity for transitions from the ground state to the excited states of an isolated dimer are proportional to:

$$
\begin{aligned}
I \propto &\langle\psi_{0,0}|\mathsf{J_{z1}}|\psi_{1,\pm1}\rangle^2 + \langle\psi_{0,0}|\mathsf{J}_{+1}|\psi_{1,\pm1}\rangle^2 + \langle\psi_{0,0}|\mathsf{J}_{-1}|\psi_{1,\pm1}\rangle^2 + \ldots \\
&\langle\psi_{0,0}|\mathsf{J_{z2}}|\psi_{1,\pm1}\rangle^2 + \langle\psi_{0,0}|\mathsf{J}_{+2}|\psi_{1,\pm1}\rangle^2 + \langle\psi_{0,0}|\mathsf{J}_{-2}|\psi_{1,\pm1}\rangle^2,
\end{aligned}
$$

where, for example, $\mathsf{J_{z1}}$ indicates the operator acts on site 1.

As a concrete example, for $|\pm\rangle = |7/2, \pm 7/2\rangle$ (which we abbreviate as $|\pm 7/2\rangle$), the first term gives,

$$\frac{1}{2}\Big(\langle 7/2|\mathsf{J_{z1}}|\pm 7/2\rangle\langle -7/2|\pm 7/2\rangle - \langle -7/2|\mathsf{J_{z1}}|\pm 7/2\rangle\langle 7/2|\pm 7/2\rangle\Big)^2 = 0,$$

since whenever the left inner product of each term (corresponding to site 1) is non-zero (for instance, in the first term, when working with the upper sign), the right inner product (corresponding to site 2) is zero. Meanwhile the second term gives,

$$\frac{1}{2}\Big(\langle 7/2|\mathsf{J_{+1}}|\pm 7/2\rangle\langle -7/2|\pm 7/2\rangle - \langle -7/2|\mathsf{J_{+1}}|\pm 7/2\rangle\langle 7/2|\pm 7/2\rangle\Big)^2 = 0,$$

since the raising operator does not connect $|-7/2\rangle$ to $|7/2\rangle$. All other terms behave similarly. Meanwhile, by similar arguments, one can see that the intensity for the transition from $\psi_{0,0}$ to $\psi_{1,0}$ is non-zero so long as there is a non-zero overlap of $\langle\pm|\mathsf{J_z}|\pm\rangle$, which is generally expected to be true except in some "accidental" cases where $\sum_{M_J} M_J|C_{M_J}|^2$ sums to zero.

The Kramer's doublet composition for $Yb_2Si_2O_7$ is currently unknown. Based on the reasoning presented here and our observation of INS intensity only in the $\psi_{1,0}$ mode, we anticipate that the doublet has relatively weak matrix elements for the raising and lowering operators (e.g. $\langle -|\mathsf{J_+}|+\rangle$) compared to $\langle\pm|\mathsf{J_z}|\pm\rangle$. However, the g-values inferred based on (nearly) saturated magnetization at $H = 5$T ($g_a* = 3.2$, $g_b* = 2.0$, $g_c = 4.8$) are not strictly Ising-like, implying there are *non-zero* matrix elements $\langle\psi_m|\mathsf{J_\pm}|\psi_p\rangle$. Thus, one may expect to be able to observe the $|\psi_{1,\pm 1}\rangle$ modes via INS with larger sample volumes.

ULTRASOUND VELOCITY MEASUREMENTS

Sound velocity measurements were performed as a function of field applied along c^* at fixed temperature (as presented in the main text) and as a function of temperature at fixed field (as presented in Fig. S1). The ultrasound velocity experiments were performed down to 50 mK using a pulsed, time-of-flight interferometer. 30 MHz transducers were glued to parallel surfaces so as to propagate longitudinally polarized sound waves along the c^*-axis. The absolute velocity of the quasi-longitudinal mode studied here was approximately 3000 m/s and relative changes in velocity ($\Delta v/v$) were measured with high precision using a phase-lock loop. Antiferromagnetic phase boundaries could be determined at low temperatures (below 150 mK) from the field sweeps by selecting a sharp change in slope (H_{c1}) and a minimum in sound velocity (H_{c2}). As the temperature is raised, these anomalies are significantly broadened and it becomes impossible to determine phase boundaries from the field sweeps. The top of the antiferromagnetic "dome" was thus determined from small anomalies (abrupt changes in slope) in the temperature sweeps shown in Fig. S1. These anomalies are entirely consistent with the peaks found in low-temperature specific heat measurements.

The inset of Fig. 4c in the main text shows a comparison of the sound velocity field sweep with the field-derivative of the neutron Bragg intensity, dI/dB, which is proportional to $d(m_z^2)/dB = 2m_z\chi$. The agreement is excellent and this suggests that the sound velocity is well coupled to the uniform longitudinal magnetization. However, a standard theoretical treatment gives a somewhat different relationship between magnetization and sound velocity. Assuming a linear-quadratic magnetoelastic coupling term in the free energy

$$F_{me} = \frac{1}{2}\kappa\epsilon_n m_z^2$$

where κ is a magnetoelastic coupling constant related to a particular element of the strain tensor, ϵ_n. Following the work of Quirion *et al.* [3], amongst others, the elastic constant is renormalized as

$$C_{mn} = \frac{\partial^2 F}{\partial\epsilon_m\partial\epsilon_n} - \frac{\partial^2 F}{\partial m_z\partial\epsilon_m}\left(\frac{\partial^2 F}{\partial m_z^2}\right)^{-1}\frac{\partial^2 F}{\partial m_z\partial\epsilon_n}$$

For the particular mode studied here,

$$C_{33} = C_{33}^0 - \left(\frac{\partial^2 F}{\partial m_z\partial\epsilon_3}\right)^2\left(\frac{\partial^2 F}{\partial m_z^2}\right)^{-1}$$

$$C_{33} = C_{33}^0 - (2\kappa m_z)^2 a^{-1} = C_{33}^0 - \kappa^2 m_z^2\chi_z$$

Relative changes in sound velocity can then be related to relative changes in elastic constant through

$$\frac{\Delta v}{v} = \frac{\Delta C_{33}}{2C_{33}^0} = -\frac{\kappa^2 m_z^2\chi}{2C_{33}^0}$$

There are thus two striking differences between this simple theory and the results. 1. As mentioned above, experimentally $\Delta v/v \propto |m|\chi$ whereas the theory predicts $\Delta v/v \propto m^2\chi$. As such, the dip at H_{c2} is less pronounced experimentally than theoretically. 2. The area under the curve $\int_0^{B_{\text{sat.}}}(\Delta v/v)dB$, which according to theory should simply give $m_{\text{sat.}}^3$, is in reality strongly temperature dependent. Hence, in the future, a more elaborate theoretical treatment of sound velocity for such a system, including coupling to the antiferromagnetic order parameter and spin fluctuations, would be valuable and might provide a more quantitative understanding of these results.

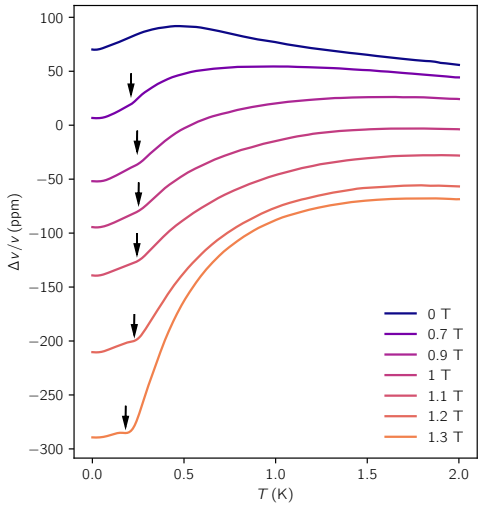

Fig. S 1: Ultrasound velocity measurements as a function of temperature at constant magnetic field. Arrows indicate anomalies associated with antiferromagnetic ordering.

SINGLE CRYSTAL NEUTRON SCATTERING

Five single crystals were co-aligned using Laue X-ray scattering to achieve an overall mass of 1.1 g and a predominant mosaic spread of less than 3°. The crystal mount is shown in Fig. S2. One of the crystals was later discovered to contain a misaligned grain, which is visible in the neutron scattering data. The elastic scattering (-0.037 meV to 0.037 meV) shows Bragg peaks from the misaligned grain, highlighted by red circles in Fig. S3. Figure S4 to Fig. S6 show inelastic slices along various reciprocal lattice directions for every applied magnetic field setting (parallel to c). At low fields, the presence of the misaligned grain is clearly observed, manifesting as what looks like an additional excitation branch in portions of the HK0 plane. It is particularly prevalent along the [-1K0] direction where the inelastic scattering from the misaligned grain is visible for negative K values (Fig. S5). The excitations of this misaligned grain are not visible for fields greater than 1.25 T. This may be due to the overall decrease in inelastic intensity which occurs due to the development of strong magnetic Bragg peaks.

Fig. S 2: The coalignment of five crystals used for the inelastic neutron scattering measurement.

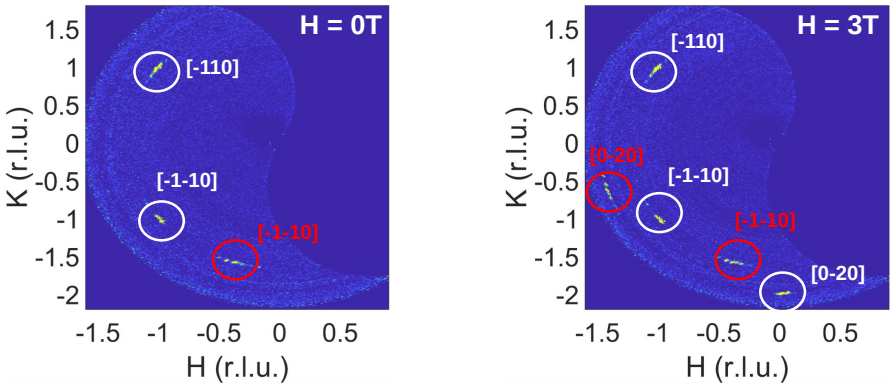

Fig. S 3: Slices taken at the elastic line (integrated from $E = -0.1$ to 0.1 meV) with E_i = 1.55 meV. Bragg peaks (both nuclear and magnetic in origin) arising from the main grain are labeled in white. Bragg peaks from the misaligned grain are circled in red. The HKL values for reflections from the misaligned grain were determined based on their 2θ values.

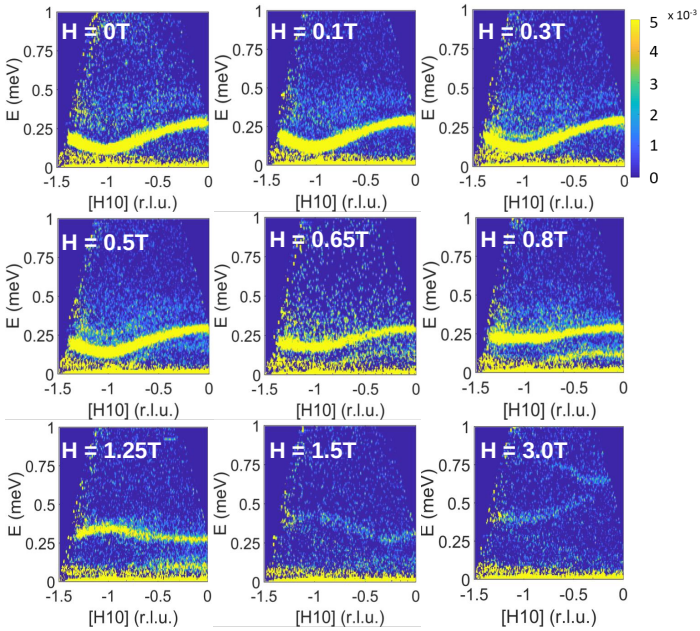

Fig. S 4: Slices along [H10] (integrated from K=0.9 to 1.1) for E_i = 1.55 meV.

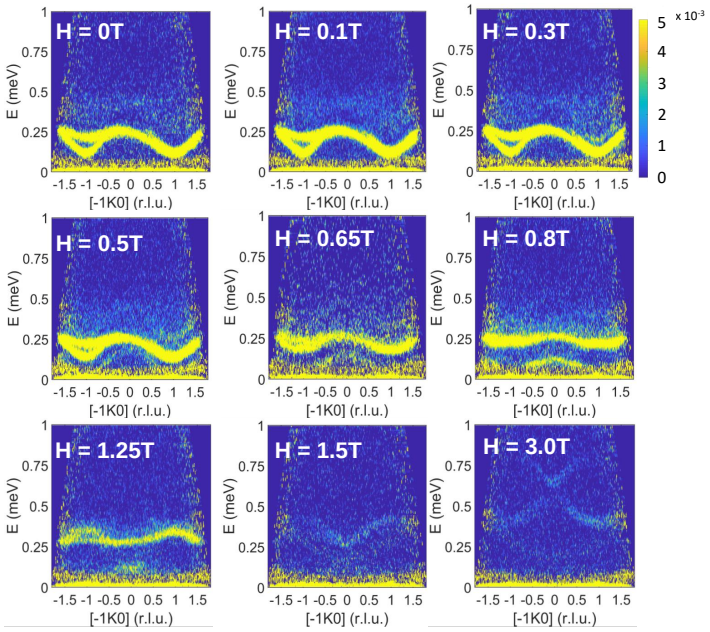

Fig. S 5: Slices along [-1K0] (integrated from H=-1.1 to -0.9) for E_i = 1.55 meV.

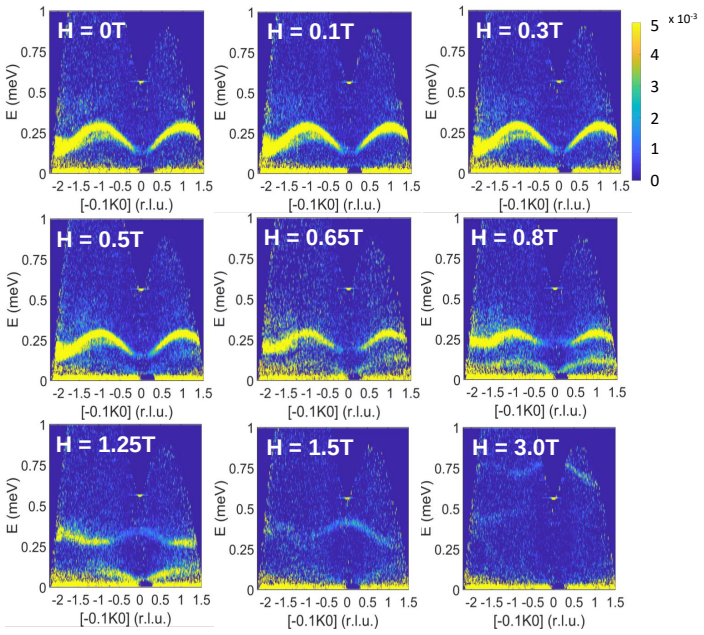

Fig. S 6: Slices along [-0.1K0] (integrated from H=-0.2 to 0) for E_i = 1.55 meV. A selection of these are shown in the main text, Fig. 4a

POWDER NEUTRON DIFFRACTION

Neutron powder diffraction data (taken on the instrument BT1 at the NIST Center for Neutron Research) confirms a lack of long range magnetic order in zero applied field. No magnetic Bragg peaks are observed at 300 mK (see the high vs. low temperature difference plot in Fig. S7).

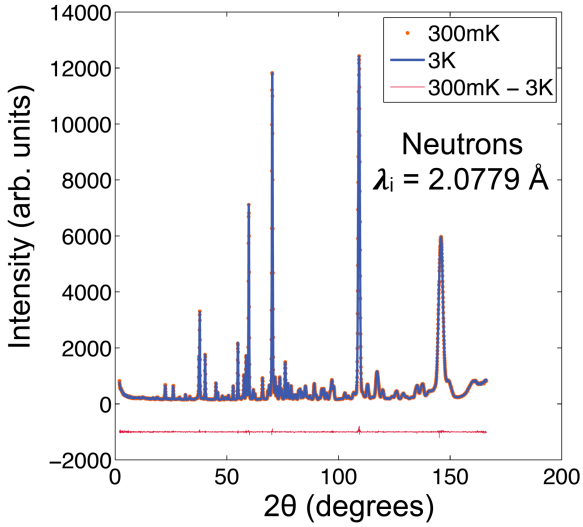

Fig. S 7: Powder neutron diffraction data taken at 300 mK and 3 K. No additional Bragg peaks are observed at 300 mK.

POWDER SYNCHOTRON X-RAY DIFFRACTION

Synchrotron X-ray powder diffraction was performed using the Advanced Photon Source at Argonne National Laboratory using the 11-BM beamline with $\lambda = 0.4122$Å. Rietveld refinement of the data agrees well with the previously published structure of $Yb_2Si_2O_7$ [4]. Refined structural parameters at 295 K are listed in Table I.

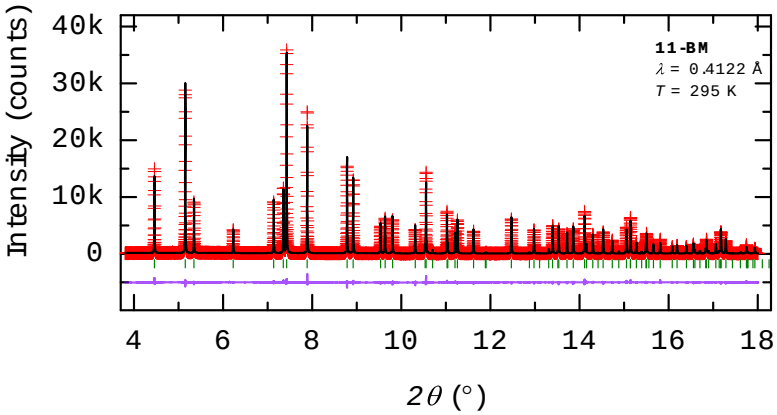

Fig. S 8: Synchrotron X-ray diffraction data measured on polycrystalline $Yb_2Si_2O_7$ at 295 K (red data points), with structural refinement (black line) and difference curve (purple line) shown.

MAGNETIZATION

Magnetization was measured at 1.8 K using a Quantum Design SQUID magnetometer, shown in Fig. S9. Proper orientation of the crystal was confirmed before and after measurements using Laue x-ray diffraction.

Atom	Site	x	y	z
Yb	$4g$	0.5	0.8066(8)	0
Si	$4i$	0.7184(4)	0.5	0.4137(6)
O	$2c$	0.5	0.5	0.5
O	$4i$	0.8804(7)	0.5	0.7215(9)
O	$8j$	0.7362(8)	0.6510(8)	0.2160(4)

TABLE I: Structural parameters at 295 K. Space group C2/m, a = 6.7714(9), b = 8.8394(2), c = 4.6896(5), β = 101.984(9).

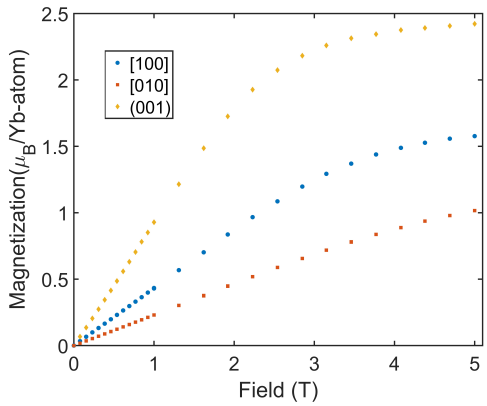

Fig. S 9: Magnetization along a^*, b^*, and c yields the g-tensor values shown in the main text, $g_{a*} = 3.2$, $g_{b*} = 2.0$, and $g_c = 4.8$.

HIGH-TEMPERATURE SPECIFIC HEAT

The magnetic specific heat of a polycrystalline sample of $Yb_2Si_2O_7$ was found by subtracting the specific heat of $Lu_2Si_2O_7$ (the non-magnetic lattice analog), and is shown in Fig. S10. The data show the field dependence of the low temperature Schottky anomaly, and also show the beginnings of a Schottky anomaly (upturn after 10 K) signaling the presence of a crystal field level at approximately 120 K. The 0T data was reproduced at both Colorado State University (using a Quantum Design Physical Properties Measurement System) and Université de Sherbrooke.

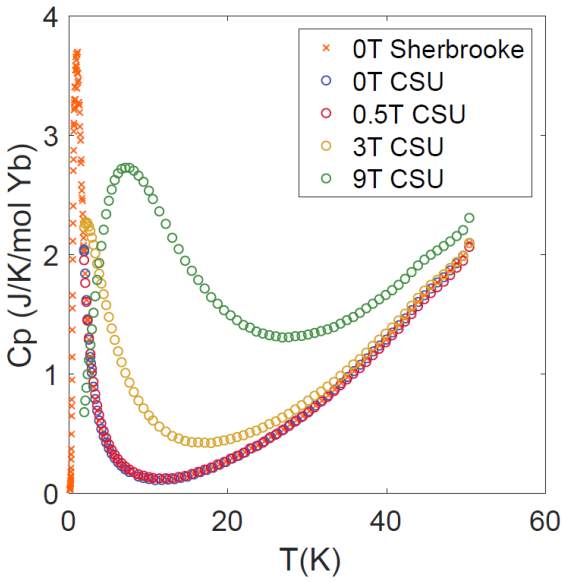

Fig. S 10: Field-dependent magnetic specific heat (lattice subtracted) from a polycrystalline sample.

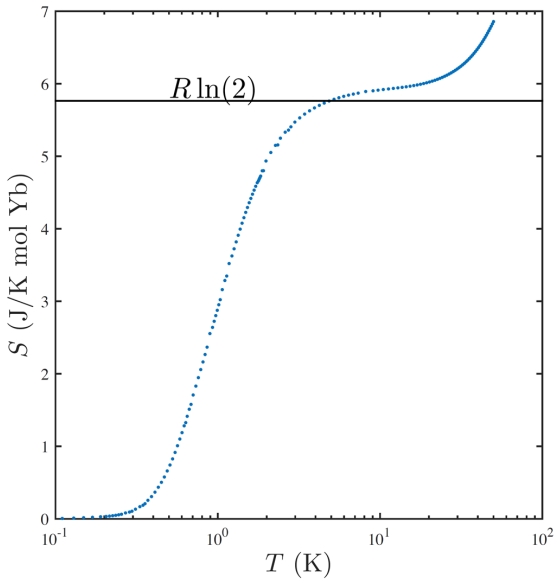

Fig. S 11: Magnetic entropy extracted from the 0T specific heat measurement. The entropy reaches Rln2 per Yb between 50 mK and 5 K, indicating a low temperature effective spin-1/2.

[1] M. Rotter, D. Manh Le, J. Keller, L. G. Pascut, T. Hoffmann, M. Doerr, R. Schedler, P. Fabi, S. Rotter, M. Banks, et al., *Mcphase users manual: Symmetry considerations for crystal field parameters*, URL http://www2.cpfs.mpg.de/~rotter/homepage_mcphase/manual/manual.html.

[2] A. Abragam and B. Bleaney, *Electron paramagnetic resonance of transition ions* (OUP Oxford, 2012).

[3] G. Quirion, X. Han, and M. L. Plumer, Phys. Rev. B **84**, 014408 (2011).

[4] J. Felsche, Journal of The Less-Common Metals **21**, 1 (1970).